Quim. Nova, Vol. 43, No. 8, 1017-1025, 2020 http://dx.doi.org/10.21577/0100-4042.20170578

Artigo

SYNTHESIS OF MATERIALS PRODUCED FROM SPENT BATTERIES WITH ENVIRONMENTAL APPLICATION

Mayra Aparecida Nascimento[a], Jean Castro da Cruz[a], Marina Ferreira dos Reis[a], Carolina Teixeira Costa Alpino[a], Cristiana Resende Marcelo[b], Guilherme Dias Rodrigues[c], André Fernando de Oliveira[a] and Renata Pereira Lopes[a,*]

[a]Departamento de Química, Universidade Federal de Viçosa, 36570-000 Viçosa – MG, Brasil
[b]Universidade Federal do Maranhão, 65700-000 Bacabal – MA, Brasil
[c]Departamento de Química, Universidade Federal de Minas Gerais, 31270-901 Belo Horizonte – MG, Brasil

Recebido em 18/12/2020; aceito em 11/05/2020; publicado na web em 30/06/2020

In this work, alkaline and nickel-metal hydride spent batteries were used as precursors of metals for the synthesis of polymetallic materials. These materials were synthesized via chemical reduction. Materials produced from nickel-metal hydride spent batteries (PM-NiMH) have a nanometric size, whereas the alkaline spent batteries (PM-Alk) have a micrometric size. PM-NiMH consists mainly of Ni, Co, and Cu and the PM-Alk consists mainly of Mn and Zn. The surface areas of PM-NiMH and PM-Alk were 82 $m^2 g^{-1}$ and 109 $m^2 g^{-1}$, respectively. The synthesized materials were applied in the removal of reactive blue dye 4 (RB4). Parameters such as initial pH of the system, dose of the materials, and initial concentration of the dye were optimized. For both materials, the removal capacity of RB4 was constant over a wide pH range of (4-10). The removal capacity increases with the decrease of the materials dose and increase of the dye concentration until saturation of the active sites. The RB4 removal by PM-NiMH occurs by adsorption and degradation processes, whereas PM-Alk occurs only by adsorptive processes. The RB4 removal process follows the Langmuir adsorption isotherm model with maximum removal capacities of 331 and 127 mg g^{-1} for PM-NiMH and PM-Alk, respectively.

Keywords: electronic waste; nickel-metal hydride spent batteries; alkaline spent batteries; value added material; removal; reactive blue 4 dye.

INTRODUCTION

The concern about the environment is paramount, especially concerning the pollution of water bodies. Therefore, the constant monitoring of industrial effluent treatment and effluents from textile industries is of fundamental importance. Several treatment processes have been used in the removal of dyes in water bodies including ceramic membrane ultrafiltration,[1] coagulation/flocculation,[2] adsorption,[3-7] photocatalytic degradation,[8] ozonization,[9] electrochemical treatment,[10] among others. Among these, adsorption is recognized as a promising method due to its simplicity of application, high efficiency and in many cases low cost, low energy consumption, and does not cause secondary pollution.[11]

A wide variety of organic materials have been used as adsorbents for dyes including chitosan,[6] kaolin and zeolite,[12] canola stalk,[13] rice husk,[14] nanodiamond,[15] ilmenite nanoparticles,[16] sepiolite clay,[5] residues of groundnut shell,[17] among others. Beyond the organic materials, wide variety materials containing metals have been used as adsorbents of dyes with promising results as Fe_3O_4 magnetic nanoparticles,[18] nanoparticles-composed Cu_2O microspheres,[3] Co_3O_4 nanoparticles,[7] nickel nanoparticles,[4] ZnO nanoparticles,[19] cobalt nanoparticles,[20] Co_3O_4–ZrO_2 composites,[21] bimetallic Fe–Zn nanoparticles,[22] ZnO nanoparticles,[23] alunite coated MnO_2.[24]

An important issue is to find new adsorbent materials to improve removal efficiency in terms of environmental decontamination. Many adsorbents as biosorbents are synthesized from some type of residue. These processes are promising and ecological because they have the advantage of using waste as a raw material, which in the case of biosorbents uses organic waste. Since materials containing metals are efficient in the removal of textile dyes, new materials can be synthesized from waste containing metals.

*e-mail: renata.plopes@ufv.br

Spent batteries in electronic waste, is an excellent source of metals that can be used as raw material. Batteries have versatile applications, low cost and are discarded in a short time. Alkaline (B-Alk) and nickel-metal hydride (B-NiMH) spent batteries constitute an example of this waste. Both batteries are widely used in portable devices used day-to-day. B-NiMH has in its composition metals such as Ni, Co, Zn, Mn, and rare earth.[25] The B-Alk are composed mostly of metals Mn and Zn.[26]

Some works in the literature report the recovery of metals from electronic waste for new materials synthesis. Shokri *et al.*[27] synthesized Cu-Sn nanoparticles from obsolete computer printed circuit boards by thermal micronizing process. Farzana *et al*.[28] synthesized MnO and ZnO from spent Zn–C battery via thermal nanosizing. López *et al.*[29] synthesized zinc oxide nanoparticles from spent alkaline batteries by selective leaching of zinc, evaporation, and calcination. Deep *et al.*[30] recovered high-purity zinc oxide nanoparticles from the waste of spent batteries alkaline. Ebin *et al.*[26] produced Zn and MnO particles from alkaline and zinc–carbon battery waste. However, these works only report the synthesis of materials without evaluating its application.

Thus, this work aimed to provide a recyclable alternative for spent alkaline batteries and spent nickel-metal hydride batteries. Thereunto, new polymetallic materials were synthesized adding value to these compounds. The new materials were characterized and, subsequently, an application was proposed for environmental decontamination, wherein reactive blue 4 dye was used as the model molecule.

MATERIALS AND METHODS

Reagents and solutions

The following reagents were used: reactive blue 4 dye (35% m/m - Sigma-Aldrich), whose chemical structure is presented in the supplementary material (Figure 1S), sodium borohydride (98% m/m

- Vetec), sulfuric acid (Alphatec), ethanol (Neon), sodium hydroxide (Neon), hydrochloric acid (Neon), citric acid (Neon), and nitric acid (Neon). All solutions were prepared using ultrapure water (Millipore Milli-Q, USA) and stored at 4 °C. All reagents used in this work were analytical grade without further purification.

Dismantling and leaching of the NiMH spent batteries

The procedure of the dismantling and leaching of the B-NiMH was performed according to the adaptations of methodology reported by Valadares *et al.*[31] Initially, the used batteries were opened with the pliers aid. The metallic casing, the plastic part, and the cardboard present in the pile were discarded. The internal material was separated and left in the chapel for about 2 hours. This material was kept in a drying oven at 60 °C for 24 hours. After drying, the material was crushed in a ring mill. In sequence, 10.00 g of the material was added to a round bottom flask with 100 mL of aqua regia leaching solution (3 HCl: 1 HNO_3, v/v). The resulting mixture was submitted to a reflux leach for 2 hours using a round bottom flask immersed in a glycerin bath under constant magnetic stirring and temperature of 65 °C. After leaching, the obtained liquor was cooled, vacuum filtered and transferred to 1.00 L volumetric flask with volume filled with ultrapure water.

Dismantling and leaching of the alkaline spent batteries

The dismantling and leaching of the material were performed according to the methodology reported by Leite *et al.*[32] The spent alkaline batteries were collected after complete exhaustion. The metallic casing, the plastic part, and the cardboard present in the pile were discarded. The internal material was separated and dried in a drying oven for 24 hours at 105 °C. Subsequently, the material was ground in a ring mill to get smaller particles. 10.00 g of the obtained material was added to a round bottom flask with 300 mL of leach solution. The leach solution was composed of 5% H_2SO_4 (v/v) and 4% H_2O_2 (v/v). The mixture was submitted to reflux leaching, which remained under constant agitation at 65 °C in a glycerin bath for approximately 2 hours. The obtained liquor was cooled, vacuum filtered, transferred to a 1.00 L volumetric flask and volume completed with ultrapure water.

Synthesis of polymetallic materials

For the synthesis of polymetallic materials, the pH of the obtained liquor was adjusted to 3.0 with a NaOH solution (10.0 mol L^{-1}). Subsequently, 100.00 mL of sodium borohydride solution (1.06 mol L^{-1}) was added, at a rate of about 0.05 mL s^{-1}, to 100.00 mL of the liquor under constant stirring. The solid material formed was vacuum filtered, washed with distilled water and ethanol, and oven-dried at 50 °C for drying. After drying, the material was stored in a freezer at -20 ± 2 °C until use.

Characterization of polymetallic materials

Different techniques were used to characterize the synthesized materials, such as:

- The NiMH materials morphology was analyzed by Transmission Electron Microscope (TEM) (Tecnai G2-20 - SuperTwin FEI - 200 kV) with a detector (EDAX) of Si-Li for Energy Dispersing X-Ray Spectroscopy (EDX) allowing an elementary analysis of the material.
- The alkaline materials morphology was analyzed by Scanning Electron Microscopy (SEM) (FIB Quanta FEG 3D FEI) and the chemical mapping of the elements present in the materials was evaluated by Electron Dispersive X-rays (EDX).
- The identification of the species presents in the materials, before and after the reaction, was performed using X-ray Diffraction (XRD) (Bruker model D8 Discover) with radiation Cu-Kα (λ = 0.1541 nm with angular variation 2θ from 5 to 95°).
- The components present in the alkaline materials were evaluated by Raman Spectroscopy (Bruker, Senterra, equipped with detector CCD, using a laser with λ = 633 nm and laser power at 2 mW).
- The specific surface area, volume, and pore diameter of the materials were analyzed using the equipment Quantachrome Autosorb 1. The measurements were carried out with 40 cycles of nitrogen adsorption and desorption degassing at 100 °C for 14 hours. The specific surface area of the PM-NiMH was calculated using the Brunauer-Emmett-Teller (BET) model and the pore volume and pore size were calculated by the Barrett-Joyner--Halenda (BJH) model.
- The point of zero charge pH (pH_{PZC}) point of PM-NiMH was determined with adaptations of the methodology reported by Calvete *et al.*[33] For this, the initial pH of the NaCl solutions (0.050 mol L^{-1}) was adjusted in a range of 2-12 using solutions of HCl (0.10 mol L^{-1}) or NaOH (0.10 mol L^{-1}). Then, 25.00 mL of the NaCl solutions at different pH values were placed in Erlenmeyer flasks with 10.0 mg of PM-NiNH. The system was submitted to constant stirring (250 rpm) over 48 hours. After this time interval, the solutions were centrifuged, and the pH of the supernatant was measured (pH_{final}). The pH_{PZC} is the point that crosses the "x" axis on the ΔpH (pH_{final} - $pH_{initial}$) versus $pH_{initial}$ curve.
- A Zeta Potential analyzer (Malvern Zetasizer Nano ZS) was used to determine the pH_{PZC} of the PM-Alk. The zeta potential was measurement at different pH values (4-12).

RB4 dye removal by PM-NiMH and PM-Alk

All the removal tests were performed in batch. The experiments were conducted in an Erlenmeyer flask, wherein 25.00 mL of RB4 solution (200.0 mg L^{-1}) was placed in contact with a certain mass of PM-NiMH or PM-Alk. The system was subjected to constant orbital stirring (250 rpm a 25 °C) in the predetermined interval. The temperature was maintained constant with a thermostatic bath (Microquímica – MQBTC 99-20). An aliquot of the solution was withdrawn, diluted in deionized water (1:20, v/v), and filtered on polytetrafluoroethylene PTFE membrane (0.45 µm, 13 mm diameter, Millipore). The residual concentration of RB4 in the aqueous solution was determined using a Molecular Spectrophotometer UV/Vis (Thermo scientific - Evolution Array). The quartz cuvette of 1 cm optical path was used, and the wavelength 257 or 599 nm was monitored. The linear range of work was verified utilizing the analytical curve (0.50 – 40.0 mg L^{-1}).

The amount of RB4 removed at equilibrium time (q_e) was calculated using Equation 1.

$$\text{Removal capacity } (q_e) = \frac{(C_0 - C_e)V}{m} \quad (1)$$

wherein C_0 and C_e are the initial and equilibrium time concentrations (mg L^{-1}), respectively. V is the volume of the RB4 solution (L), and m is the mass of materials (g).

The reaction conditions were evaluated through some parameters such as (1) initial pH of the solution (2.0 – 12.0), which was adjusted with HCl (1.0 mol L^{-1}) or NaOH (1.0 mol L^{-1}) solutions; (2) dosage of PM-Alk (0.40 – 1.60 mg g^{-1}), and (3) concentration of the RB4 (200.0 – 1000.0 mg L^{-1}). The experimental data were adjusted to

the Langmuir, Freundlich, Temkin, and Dubinin–Radushkevich isotherm models.

All experiments were performed in replicate and the mean of the results was reported along with their standard deviation.

Desorption assays of RB4

Desorption experiments were performed using citric acid (0.01 mol L^{-1}) for PM-NiMH and sodium hydroxide (0.075 mol L^{-1}) for PM-Alk. For these assays, after reaction with the dye, the materials were centrifuged and washed with distilled water three times and added to 20.00 mL of the extractive solutions under orbital shaking (250 rpm). Subsequently, aliquots were withdrawn, diluted, filtered (PTFE membrane, pore size 0.45 µm, Millipore). The pH was adjusted to approximately 8.0 and the concentration of RB4 was determined by Molecular Spectrophotometry UV/Vis.

RESULTS AND DISCUSSION

Characterization of materials

Morphological analysis by Microscopy

Materials obtained after chemical reduction with sodium borohydride were characterized by TEM (PM-NiMH) and SEM (PM-Alk), as can be seen in Figure 1.

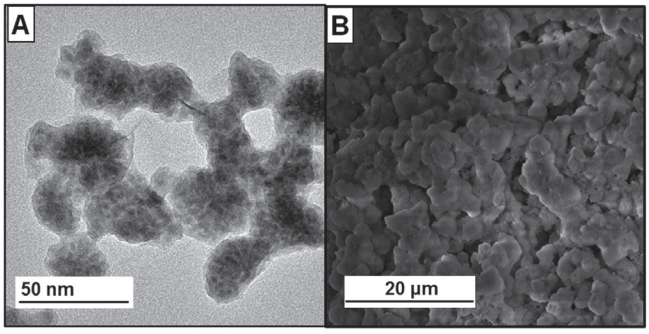

Figure 1. *(A) Images obtained by Transmission Electron Microscopy (TEM) of PM- NiMH. (B) Images obtained by Scanning Electron Microscopy (SEM) of PM-Alk*

PM-NiMH has a spherical shape with a nanometer-sized diameter. As can be seen in Figure 1A, small spheres agglomerate to form larger spheres smaller than 50 nm size. In these larger spheres, it is possible to observe a kind of pores, due to the way nanomaterials have clustered. PM-Alk has irregular shape and micrometric scale size as can be seen in Figure 1B. Both materials form agglomerates as can be seen in Figure 1. Agglomeration is observed in several works where metallic materials are used.[4,18,22]

From the EDX spectrum (Figure 2S), it was possible to verify that PM-NiMH are formed predominantly by metals Ni, Cu, and Co. Other elements are also present such as Zn, Mn, Tl, Si, and internal transition metals such as La and Ce. A peak of oxygen was also identified, which is attributed to oxides present on the material surface. From the chemical mapping (Figure 3S), it was possible to observe that the PM-Alk are basically composed of Mn, Zn, and Fe and homogeneously distributed over the material structure.

The obtained results are consistent with data reported in the literature. B-NiMH are composed of several types of metals and some works have promoted the recovery of these metals. Gramata *et al.*[34] analyzed the dust resulting from mechanical treatments of B-NiMH and verified that are composed of Ni, Mn, Li, Fe, Co, Cu, Al, Ce, La, and Nd. Meshram *et al.*[25] performed the extraction of the metals present in the cathode and anode of B-NiMH and recovered some metals such as Ni, Co, Zn, Mn, and rare earth elements such as La, Ce, Nd, Pr, and Sm. Rodrigues and Mansur[35] determined the metal composition of B-NiMH and identified the following metals: Al, Cd, Co, Ce, Fe, Hg, K, La, Mn, Nd, Ni, Pb, Pr, Ti, and Zn. Besides these metals, the present work detected the presence of copper metal. According to Vassura *et al.*,[36] the batteries electrical joints can be made of metals such as copper. According to Ebin *et al.*,[26] the metals Mn and Zn correspond to 28 ± 1 and 25 ± 1% (m/m), respectively, of the internal composition mass of the B-Alk after mechanical treatment. Some elements that may be present in the B-Alk composition such as K, Cl, and C,[29] are not reduced by borohydride and therefore, were eliminated in the washing and filtration step of the materials.

Structural analysis

X-ray diffraction analysis was performed to better understand the crystalline structures of the materials. For PM-NiMH (Figure 2), peaks can be observed in values of 2θ in 43.94°, 50.35°, and 74.22° corresponding to the planes (111), (200), and (220), respectively, which were assigned the face-centered cubic Ni structure (JCPDS 89-7128), Co (JCPDS 89-4307), and Cu (JCPDS 89-2898). Also, there were small deviations of all values of 2θ, suggesting a corresponding increase in the network parameters, which is observed in the magnification of the plane (111) in Figure 2B. There is a 2θ offset for lower angle values compared to the crystal face (111) of the pure Ni, Co, and Cu reference standards. The 2θ values of Ni,

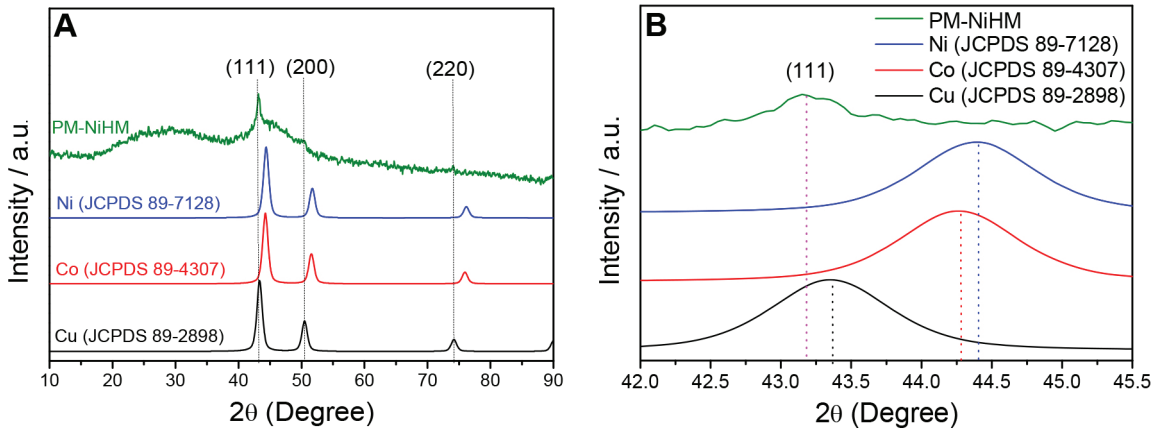

Figure 2. *(A) X-ray diffractogram of PM-NiMH and diffractograms references of Ni, Co, and Cu (B) Enlarged view of the peaks corresponding to the plane (111) of the prepared PM- NiMH and Ni, Co and Cu references*

Co and Cu pure corresponding to the plane (111) are 44.40°, 44.28°, and 43.36° respectively.

The network parameters (a) were calculated according to Equation 2, and the results can be seen in Table 1S.

$$a = \frac{\lambda}{2\ \mathrm{sen}\theta}\sqrt{h^2 + k^2 + l^2} \quad (2)$$

wherein λ is the X-ray diffraction wavelength, 0.15406 nm; 2θ is the position of the diffraction peak (111) in the XRD standards; and h, k, l are the Miller indices.

As can be observed in Table 1S, the network parameters increased from 0.3531 to 0.3626 nm compared to pure nickel due to the interaction with cobalt and copper with a higher atomic radius, suggesting the formation of a trimetallic alloy. Similar results were reported by Chen *et al.*,[37] Hu *et al.*[38] and Lua and Wang.[39]

After the dye removal process by PM-NiMH, the materials were also characterized by X-ray diffraction. As can be seen in Figure 4S, all peaks observed before the reaction also appear after the reaction with the dye, but with lower intensities. These peaks can be seen in 2θ values of 43.94°, 50.35°, and 74.22°. Also, new peaks with values of 2θ of 33.90°, 43.28°, 60.74°, 74.22°, and 77.73° appeared corresponding to the crystalline planes (111), (200), (220), (311), and (222), respectively, which can be attributed to the metal oxides of the NiO nanomaterials composition (JCPDS 78-423), CoO (JCPDS 78-431) and CuO (JCPDS 78-428). It can be inferred that Ni, Co, and Cu metals oxidized during the dye removal process. Also, all peaks changed by 2θ for smaller angle values, suggesting that the network parameter increases, as can be seen in Table 1S. The increase in the net parameter can be explained by a combined effect due to the formation of defects related to the oxygen vacancies inside the oxide network and the metallic Ni, Co and Cu radius much larger than the Ni^{2+}, Co^{2+}, and Cu^{2+}.[40]

For the PM-Alk, it was possible to observe from the X-ray diffraction results (Figure 3A) that the material is amorphous since it was not possible to identify diffraction peaks. Only a broad peak in the region of 2θ = 25° is observed, which can be attributed to the support used for the analysis (glass slide). Probably, during the synthesis, the different metals were not arranged of regular form, being not possible the formation of crystals. Thus, for this material, the Raman analysis was performed to verify the vibrational modes related to the phases of the metals present in the PM-Alk, as observed in Figure 3B.

The two bands in the region of 323 and 380 cm^{-1} (Figure 3B) may be associated with manganese oxide hausmannite (Mn_3O_4), with symmetry of type E_g and T_{2g}, respectively, as observed by Mironova-Ulmane *et al.*[41] and Farzana *et al.*,[28] also identified the Mn_3O_4 band which was attributed the Raman laser oxidation of MnO to 514 nm. Thus, the identified bands may be from the Mn_3O_4 present on the surface of the microparticles, or from the MnO that was oxidized by Raman laser.

No bands were identified for zinc oxide. Possibly, the presence of Mn in the sample destroys the crystalline structure of ZnO. This may be associated with the formation of Mn agglomerates on the material surface and the generation of vacancies in the crystalline lattice. This cause a decrease in the vibrational energy of the Zn-O bonds of type E_2 symmetry, resulting in amorphous ZnO.[42] A broadband in the range between 500 and 700 cm^{-1} is a contribution of ZnO and MnO_2,[43] besides confirming the incorporation of Mn to ZnO, as reported by Silambarasan *et al.*[44] The absence of vibrational modes related to iron may be related to the small amount present in the material, as observed in the XRD results.

Sodium borohydride was added to the system to reduce the metals to their zero-valent form. For PM-NiMH, the metals were reduced to their zero-valent form as observed in the X-ray diffraction. However, for PM-Alk, it was not possible to identify Zn^0 and Mn^0 in the X-ray diffractogram, since the synthesized material is amorphous.

The reduction of Zn^{2+} and Mn^{2+} ions is thermodynamically favorable, especially for zinc, as can be observed in Equations 3 - 4. It is worth mentioning that the synthesis of zero Zn nanoparticles by zinc reduction process via sodium borohydride is described in the literature (Eq. 5).[45] It is believed that the metals in the form zero were formed, but when in contact with the atmospheric oxygen there was the oxide film formation on the material surface.

$$Zn^{2+}_{(aq)} + 2e^- \rightleftharpoons Zn^0_{(s)} \qquad E° = -0.76 \quad (3)$$

$$Mn^{2+}_{(aq)} + 2e^- \rightleftharpoons Mn^0_{(s)} \qquad E° = -1.19 \quad (4)$$

$$Zn^{2+}_{(aq)} + 2BH^-_{4\,(aq)} + 6H_2O_{(l)} \rightarrow Zn^0_{(aq)} + 2B(OH)_{3(aq)} + 7H_{2\,(g)} \quad (5)$$

Point of zero charge

The pH_{PZC} was also investigated since the pH of the solution has significant effects on the adsorbent surface charge. As can be seen in Figure 4A, the point of zero charge of PM-NiMH occurs at pH 8.6. Thus, in solution with pH values below 8.6, the PM-NiMH are positively charged and at pH values above 8.6, the materials are negatively charged. The PM-Alk showed anomalous behavior since at pH values 2 to 6, the zeta potential of PM-Alk is very close to zero. At pH values 6 to 8.4, the material has a positive zeta potential. At

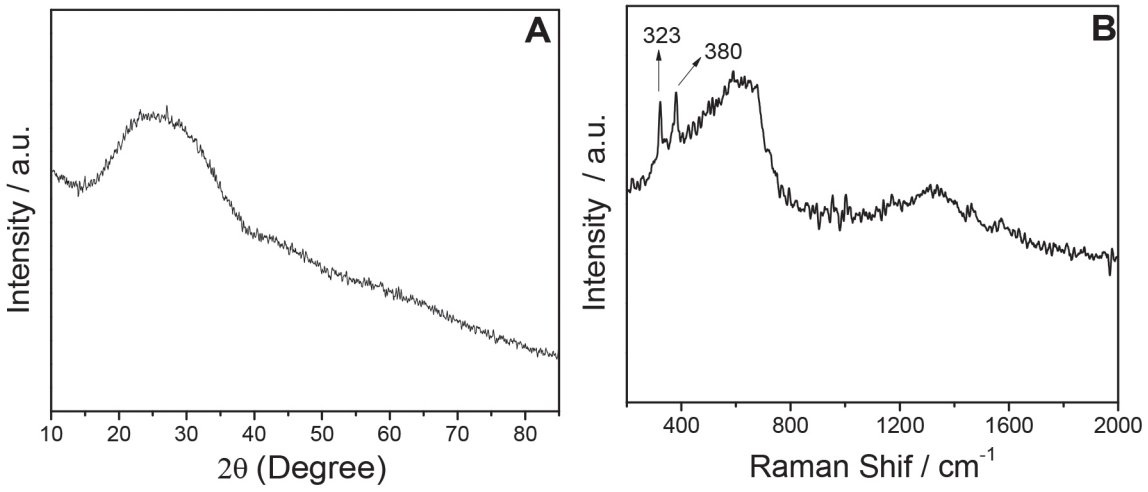

Figure 3. *(A) X-ray Diffractogram and, (B) Raman Spectrum of PM-Alk*

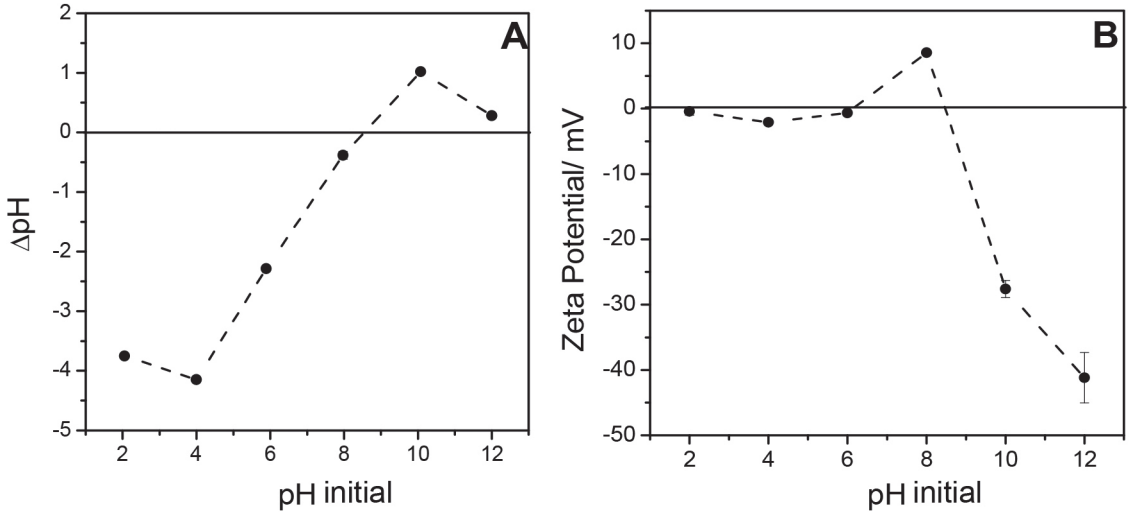

Figure 4. *Point of zero charge. (A) PM- NiMH; (B) PM-Alk*

pH values above pH 8.5, the zeta potential of the material is negative. In this way, the pH_{PZC} of the material was defined as 8.5 since it can be better evidenced by the graph. The pH_{PZC} value of the PM-Alk found is close to those found in the literature. Li *et al.*[46] determined the isoelectric point of nanoparticles of Mn_3O_4@ZnO being 9.3

Surface area

To determine the surface area of the materials, adsorption and desorption studies of N_2 were made. As can be seen in Figure 5, the isotherms for both materials can be classified as type IV with an H1 type hysteresis loop. According to the IUPAC classification, the material is mesoporous, with narrow cylindrical pore shapes or agglomerates of uniform compact beads. For the PM-NiMH, a narrow hysteresis was observed in the range of 0.60 to 0.90 (P/P_0). In the PM-Alk, it was observed that the desorption occurs at a pressure very close to the adsorption, giving a small hysteresis.

According to the pore size distribution of PM-Alk (Figure 5S), the pore sizes are distributed in a range of 8 to 60 nm for the PM-Alk and 3.5 to 30 nm for the PM-NiMH. The pore size is 4.5 for PM-NiMH and 5-15 nm for PM-Alk, confirming that the materials are mesoporous.

The specific surface area of the materials was calculated by method Brunauer, Emmett, and Teller (BET), and the volume and diameter of the pores were calculated by method Barrett, Joyner, and Halenda (BJH), as seen in Table 1.

Table 1. Specific surface area, pore volume, and pore diameter for PM-NiMH and PM-Alk

	Surface area / (m^2 g^{-1})	Pores volume / (cm^3 g^{-1})	Diameter pores / nm
PM-NiMH	82.0	0.124	4.50
PM-Alk	109	0.497	12.5

PM-Alk has a larger surface area than PM-NiMH, and higher than other similar materials reported in the literature. Farzana *et al.*[28] synthesized ZnO and MnO with surface areas equal to 9.26 and 9.63 m^2 g^{-1}, respectively. Bimetallic nanoparticles of Fe-ZnO obtained by Gautam *et al.*[22] have a surface area of 73.08 m^2 g^{-1}. Nanoparticles of hollow core ZnO obtained by Lan *et al.*[23] presented surface area of 31.04 m^2 g^{-1}. Nanoparticles of ZnO obtained by Tzvetkov *et al.*[47] presented an area of 40 m^2 g^{-1}.

It is believed that PM-Alk are composed of manganese oxides species, zinc oxides, and Zn^0. In this way, the specific surface area is larger due to the mode these species are interacting. The interaction between these different compounds should be weak, leaving void spaces between them, which provides a greater specific surface area. A similar result was obtained by Li *et al.*,[46] which found a specific surface area of Mn_3O_4 nanoparticles of 54.3 m^2 g^{-1}, while

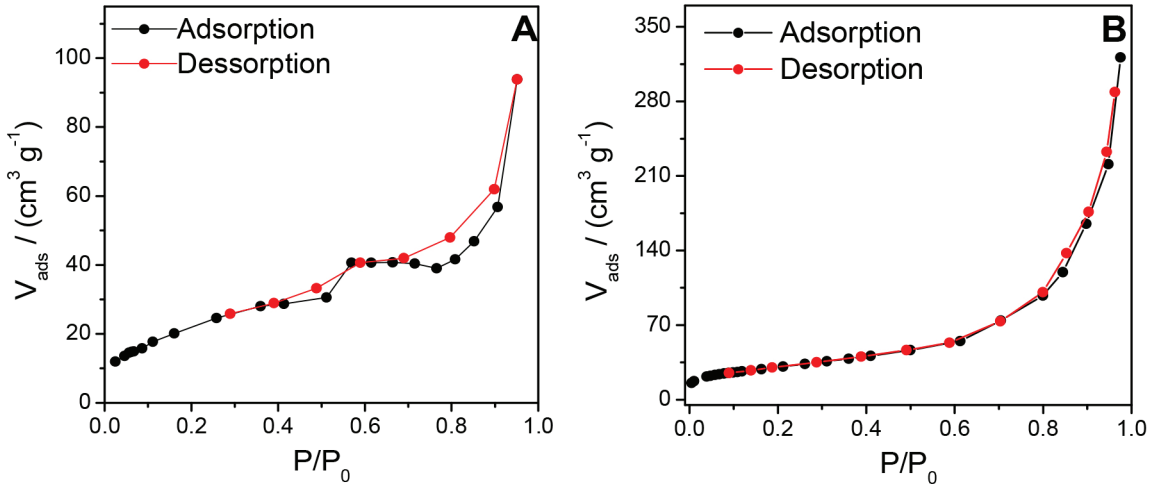

Figure 5. *N_2 adsorption/desorption isotherms for the (A) PM- NiMH and (B) PM-Alk*

the area of compound Mn_3O_4@ZnO was considerably higher, equal to 98.0 $m^2 g^{-1}$. This last one is close to that found in this work. The authors attributed this phenomenon to a weakening in the aggregation of the particles after the deposition of a ZnO layer on the Mn_3O_4 surface.

Although the surface area of the PM-NiMH is smaller than the area of the PM-Alk, is larger than the similar materials reported in the literature. Huang *et al.*[48] synthesized Cu^0 nanoparticles with a surface area of approximately 19 $m^2 g^{-1}$. Tabrizian *et al.*[49] synthesized Fe/Cu nanoparticles with an area equal to 65.88 $m^2 g^{-1}$. Lara-Vásquez *et al.*[50] synthesized Fe/Cu nanoparticles with a surface area of 63.81 $m^2 g^{-1}$.

Application of polymetallic materials in the removal of RB4

PM-NiMH and PM-Alk were applied in the removal of RB4. The spectra in the UV-Vis region can be seen in Figure 6.

In Figure 6A are shown the spectra of the RB4 solution obtained at different time intervals of contact with the PM-Alk. It can be observed that with increasing contact time, the intensities of the characteristic bands of the dye (wavelength 257 and 599 nm) decrease by about 40% in 5 hours of reaction. The spectra of the dye only decrease in intensity. There is no band shift or new appearance, which indicates that the removal of RB4 by PM-Alk occurs through adsorption. This phenomenon also was observed by visual inspection of the material. Before the process, the PM-Alk has a beige initial coloration and after the reaction has a blue coloration.

PM-NiMH is also able to remove RB4 by adsorption. Before the reaction the materials have a black coloration and after have a blue coloration. However, besides adsorption, the degradation process also was observed. Figure 6B shows the molecular absorption spectrum of dye solution after the process with 100% removal (Figure 6B). As can be seen, there is no signal at 599 nm, which is the region corresponding to the chromophore group of the molecule, i.e., when the solution loses color. However, a new peak at 212 nm is observed, which was attributed to degradation product.

The RB4 degradation by PM-NiMH occurs due to the Cu^+ species, released in the medium by the oxidation of Cu^0. This phenomenon was also observed by Marcelo *et al.*[51] and Dong *et al.*,[52] wherein Cu^+ was one of the species responsible for the removal of azo dyes since it reacts with the molecule forming carbonic radicals that are further decomposed by •OH also produced *in situ*. Since PM-Alk does not have Cu in its composition, the degradation process was not observed in the presence of this material.

To verify if adsorption was occurring, desorption assays were performed after the reaction. It was possible to desorb about 95 and 90% of the dye adsorbed by PM-Alk using, respectively, NaOH (0.075 mol L^{-1}) and citric acid (0.01 mol L^{-1}).

The ability of PM-Alk to adsorb RB4 is due to the presence of manganese and ZnO oxides in their composition since these materials have adsorbent properties as reported in the literature. Li *et al.*[46] synthesized a Mn_3O_4@ZnO/Mn_3O_4 material to remove Cr(VI) and Cr(III) by adsorption and photocatalysis process. Kataria *et al.*[19] used flower shaped zinc oxide nanoparticles to adsorb the blue dye victory B. Zhang *et al.*[53] used ZnO nanoparticles to adsorb anionic and cationic dyes.

Zero-valent zinc can degrade/reduce pollutants such as 1,2,3-trichloropropane[54] and methyl orange.[55] However, in the present work, Zn^0 was not exposed to promote the dye degradation, since Zn^0 undergoes corrosion in water forming a layer of oxide and/or hydroxide on its surface.[56] These passive species were also identified by Salter-Blanc and Tratnyek[54] which identified that the Zn^0 surface in deionized water is coated by a layer of ZnO and $Zn(OH)_2$ at pH values of 6.8, 9.6, and 11.9. Thus, since Zn^0 is not exposed, the species of oxides and/or zinc hydroxide promote the adsorption of the RB4.

However, the PM-NiMH consists of zero-valent Ni, Co, and Cu metals that keep more internally with layers of metal oxides on its surface. These zero-valent metals, together with the oxides, are the species responsible for the adsorption of the RB4 dye. Other works in the literature report some of the species present in PM-NiMH that have adsorbent properties, such as Ni,[4] Co,[20] bimetallic Cu/Co nanoparticles,[11] NiO and CuO,[57] NiO.[58]

Effect of different parameters that interfere removal process of the RB4 dye by PM-NiMH and PM-Alk

Several factors to present an important role in the removal process, such as contact time, initial pH of the medium, dose of materials and concentration of the dye. Therefore, these factors must be evaluated to obtain maximum efficiency in the removal process.

First, the equilibrium time of the dye removal by PM-Alk and PM-NiMH was determined. For the PM-Alk (Figure 6S), most of the dye was removed from the solution within 30 minutes of reaction. After the first 30 minutes, the dye removal continues, however, more slowly until equilibrium is reached in about 3 hours. For PM-NiMH,

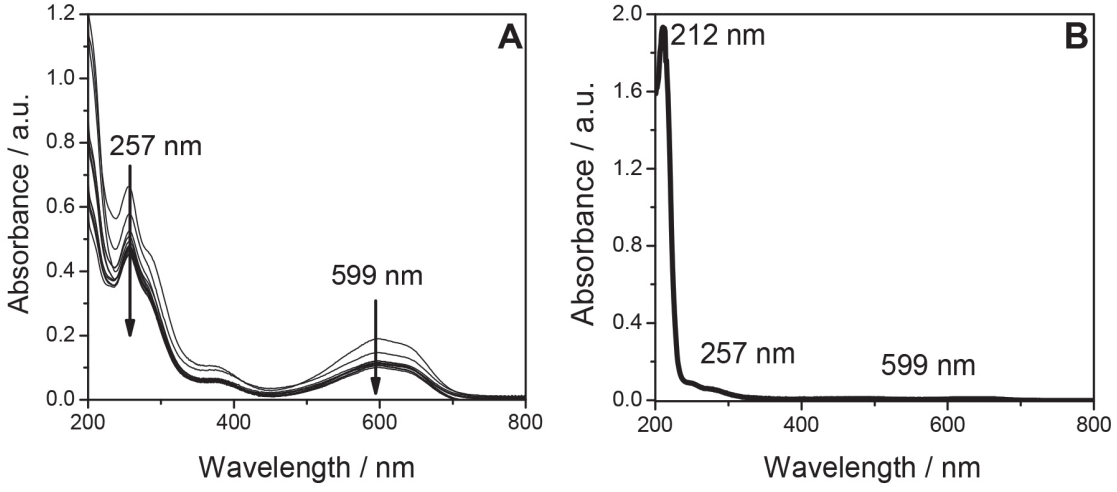

Figure 6. *(A) UV/Vis spectra of RB4 dye before and after reaction with PM-Alk with 1/20 dilution. (B) UV/Vis spectra of RB4 dye after reaction with PM-NiMH without dilution. Experimental Conditions: C_0 RB4 = 200.0 mg L^{-1}, V = 25.00 mL; temperature = 25 ºC; dose of PM-Alk = 0.40 g L^{-1}; dose of PM-NiMH = 0.80 g L^{-1}; time interval for PM-Alk 5 hours; time interval for PM-NiMH 14 hours*

rapid removal of the dye occurs in the first 3 hours of reaction. After the first 3 hours the removal continues however, more slowly until approximately 12 hours, the moment the system reaches equilibrium.

In the initial adsorption stage, all the active sites on the adsorbent surface are available, which makes the removal process fast. As the process continues, the number of vacant active sites decreases and initiates a repulsion between the adsorbate molecules adhered to the adsorbent and the solution. Once the equilibrium is reached, the adsorption and desorption rates are the same, with no apparent increase in the removal capacity.

To have greater reliability than the equilibrium was reached, the 5 and 14 hours times for the PM-Alk and PM-NiMH materials, respectively, were chosen for the later assays. After determining the adsorption time, other parameters were evaluated for both materials, and the results can be observed in Table 2.

According to Table 2, for both materials studied it is possible to observe that the best results were obtained without initial pH adjustment (pH = 3.4). In the pH range of 4-10, there is a very subtle variation in the removal capacity. This is because regardless of the initial system pH, in this range, the pH tends to rise to a buffer region at pH close to 8.4 (Figure 7S). One of the justifications for the increase in pH is due to the oxidation reactions of the species present in the materials in water, such as Ni^0, Cu^0, Co^0, and Zn^0, which release electrons in the medium. Thus, the reduction of oxygen dissolved in water releases OH^- in the medium, as observed in Equation 6. The buffer region occurs due to the species formed in the system. Probably, hydroxy complexes of Ni, Co, Cu, and Zn elements.

$$O_{2(g)} + 2H_2O_{(l)} + 4e^- \leftrightharpoons 4OH^-_{(aq)} \qquad E^0 = +0.40V \qquad (6)$$

According to *ACD/Labs*, the pKas for RB4 are -1.5, 0.5, 3.4, and 5.4. In addition to these pKas values, a fifth pKa value of 11.33 was identified through *Chemicalize*. Thus, at the final of the reaction for both materials, the dye has a negative charge, as can be observed in the effective charge graph (Figure 8S). Since the pH_{PZC} of the PM-NiMH and PM-Alk are 8.6 and 8.5, the materials have a positive or a neutral charge at the final of reaction. Thus, the electrostatic attraction may favor the removal process. However, other phenomena, such as complexation chemisorption, may also be involved in the adsorption process. Since the complexation of RB4 with PM-NiMH and PM-Alk can occur through the amino and carbonyl groups attached to the anthraquinone group present in the dye molecule.

At more extreme pH values such as 2 and 12, the removal capacity decreases for both materials. At initial pH 2, the removal capacity decreases because the materials are digested, thus reducing the adsorbent mass. This fact was observed visually during the reaction. At pH 12, the removal capacity decreases due to the loads present on the surface of the material and the dye, since at the final reaction pH both have a negative charge, which causes an electrostatic repulsion. The same phenomenon was observed by Uddin and Baig[7] which also observed that from pH 8 there is a gradual decrease in the rate of adsorption up to pH 12. The authors attributed this result to be due to precipitation and competition between hydroxyl ions and methyl orange dye on the surface of Co_3O_4 nanomaterials.

The influence of the dose was also studied. For both materials, the higher dose of the materials promotes a lower removal capacity (Table 2). This phenomenon can occur because in higher doses occurs the overlap of the available surface area of the material. Thus, the total effective surface area can decrease thus decreasing the adsorption capacity at higher doses.[59]

The variation of the initial dye concentration is also a factor that affects its removal by materials. As can be seen in Table 2, the dye removal ability for PM-NiMH increased with increasing concentration. The adsorption capacities increase with increasing initial concentration until the saturation of the adsorption sites is reached.[53] For PM-NiMH, from the concentration of 300.0 mg L^{-1}, the removal capacity is practically constant since the active sites of the material have already been saturated. In the case of PM-Alk, the adsorption capacity presented a low change in the concentrations of 200.0 - 400.0 mg L^{-1}, indicating that from the concentration of 200.0 mg L^{-1} the active sites of PM-Alk were already saturated with the dye.

Adsorption isotherms

The adsorption isotherms models are used to justify the adsorption or interaction behavior between the liquid phase and the solid phase in the system.[19] In this work, the Langmuir, Freundlich, Temkin, and Dubinin-Radushkevich (D-R) isotherm models were applied to the experimental data. The parameters can be seen in Table 3. All the isothermal parameters were calculated from the slopes and intercepts of the straight lines obtained by the linearized models (Table 2S).

The quality of the adjustment was evaluated by the determination coefficients, and it was possible to verify that the Langmuir model was better fitted to the experimental data. This model proposes that the adsorption process occurs on a homogeneous monolayer surface with no interaction between the adsorbed species, the adsorption energy is evenly distributed and the adsorbent has a finite number of adsorption sites.[60]

Table 2. Influence of the factors initial pH, material dose, and initial concentration of the dye in the removal of RB4 from the materials

			pH				
q_e / (mg g^{-1})	2	4	6	8	10	12	Without adjustment*
PM-NiMH	39.3	285.3	226.2	250.0	209.2	97.1	348.8
PM-Alk	26.5	71.2	69.1	62.8	57.6	4.8	73.6
			Dose / (g L^{-1})*				
q_e / (mg g^{-1})	0.40	0.60	0.80	1.6			
PM-NiMH	348.8	278.7	237.9	123.9			
PM-Alk	240.6	190.6	171.8	93.9			
			Concentration / (mg L^{-1})*				
q_e / (mg g^{-1})	200.0	300.0	400.0	600.0	1000.0		
PM-NiMH	233.2	316.7	303.4	296.4	266.5		
PM-Alk	174.7	171.5	170.3	149.9	130.8		

* pH without adjustment = 3.4.

Table 3. Parameters of Langmuir, Freundlich, Temkin and Dubinin-Radushkevich isotherms for adsorption of RB4 by PM-NiMH and PM-Alk

Models		Parameters		
		K_L / (L mg^{-1})	q_{max} / (mg g^{-1})	R^2
Langmuir	PM-NiMH	20.48	331.1	0.9932
	PM-Alk	0.0223	126.6	0.9925
		K_F / (L g^{-1})	$1/n_F$	R^2
Freundlich	PM-NiMH	87.76	0.2165	0.8776
	PM-Alk	284.7	0.1056	0.7058
		K_T / (L g^{-1})	b / (kJ mol^{-1})	R^2
Temkin	PM-NiMH	2.433	0.054	0.8953
	PM-Alk	4.83×10^6	0.1530	0.7255
		K_{DR} / (mol^2 kJ^{-2})	q_{DR} / (mg g^{-1})	R^2
D–R	PM-NiMH	0.0083	328.7	0.9535
	PM-Alk	90.74	152.8	0.0305

*Where K_L is the interaction constant between adsorbent and adsorbate (L mg^{-1}); q_{max} is the maximum adsorption capacity (mg g^{-1}); 1/n is the constant related to surface heterogeneity; K_F (L g^{-1}) is the Freundlich adsorption capacity constant, b (kJ mol^{-1}) is a constant associated with the heat of sorption, K_T (L g^{-1}) is the isothermal constant of Temkin, q_{DR} (mg g^{-1}) and K_{DR} (mol^2 kJ^{-2}) represent the isothermal constants of Dubinin-Radushkevich.

The maximum adsorption capacity is a parameter widely used to evaluate and compare the performance of different adsorbents. From the Langmuir model, it was possible to calculate the maximum adsorption capacity of the dye as equal to 331 and 126.6 mg g^{-1} for PM-NiMH and PM-Alk respectively. As can be observed, PM-NiMH showed a higher removal capacity than PM-Alk, because these materials have a nanometer size and are more dispersed in solution when compared to PM-Alk.

In other works, involving dyes adsorption by materials similar to PM-NiMH and PM-Alk, the Langmuir model was also the best fit. For example, the adsorption of methyl orange by manganese ferrite and hausmannite magnetic nanoparticle,[59] adsorption of malachite green and congo red dyes by bimetallic Fe-Zn nanoparticles,[22] adsorption of malachite green, acid fuchsin and congo red dyes by ZnO nanoparticles,[53] adsorption of the reactive orange 13 by MnO_2 coated alunite,[24] adsorption of crystal violet, eosin Y and orange II dyes by nickel nanoparticles.[4]

The synthesized materials showed a satisfactory removal capacity when compared to other materials used in the removal of RB4: Activated carbon developed from enteromorpha prolifera q_{max} = 131.9 mg g^{-1},[61] mustard stalk q_{max} = 25.8 mg g^{-1},[62] 3-aminopropyl triethoxysilane modified chitosan beads q_{max} = 433.8 mg g^{-1},[63] chitosan hydrogel beads impregnated with hexadecylamine q_{max} = 454 mg g^{-1}.[64]

CONCLUSIONS

It can be concluded that it was possible to synthesize satisfactorily new materials from nickel-metal hydride spent batteries and alkaline spent batteries, adding value to the new material. PM-NiMH materials were nanometric in size, mainly consisting of Ni, Co, and Cu metals and a surface area of 82.1 m^2 g^{-1}. The PM-Alk presented micrometric size being constituted mainly by metals Mn and Zn and surface area equal to 109 m^2 g^{-1}. The point of zero charge for both materials was close, being equal to 8.6 and 8.4 for PM-NiMH and PM-Alk, respectively. Through the pH assays, it was possible to conclude that one of the phenomena involved in the removal process is the adsorption by electrostatic attraction. Besides, chemisorption by complexation can also be involved in the adsorption process. The results indicated that the Langmuir model provided the best correlation with the experimental data, with a maximum adsorption capacity of 331 mg g^{-1} and 126.6 mg g^{-1} for PM-NiMH and PM-Alk, respectively.

Finally, the results obtained of the synthesis of polymetallic materials from spent batteries presents an environmentally effective approach since it provides an alternative to recycling spent batteries and its application in the textile dyes removal in the aqueous system. It is believed that the synthesized polymetallic materials can be used in other areas, including the removal of different environmental contaminants. However, additional studies should be performed to evaluate other possible applications of the synthesized materials.

SUPPLEMENTARY MATERIAL

Additional information on the characterization of PM-Alk and PM-NiMH and the results obtained in the removal of RB4 by materials is available at http://quimicanova.sbq.org.br, in the form of a PDF file, with free access.

ACKNOWLEDGEMENTS

This work was supported by the Coordenação de Aperfeiçoamento de Pessoal de Nível Superior - Brasil (CAPES) - Finance Code 001, Conselho Nacional de Desenvolvimento Científico e Tecnológico (CNPq), Fundação de Amparo à Pesquisa do Estado de Minas Gerais (FAPEMIG), CNPq/FAPEMIG (agreement recorded in SICONV: 793988/2013). We thank also acknowledge the Microscopy Center at the Federal University of Minas Gerais (http://www.microscopia.ufmg.br) for providing the equipment and technical support for the experiments involving electron microscopy.

REFERENCES

1. Alventosa-deLara, E.; Barredo-Damas, S.; Alcaina-Miranda, M. I.; Iborra-Clar, M. I.; *J. Hazard. Mater.* **2012**, *492*, 209.
2. Zahrim, A. Y.; Hilal, N.; *Water Res. Ind.* **2013**, *3*, 23.
3. Liao, H.; Wang, Z.; *J. Alloys Compd* **2018**, *769*, 1088.
4. Pandian, C. J.; Palanivel, R.; Dhananasekaran, S.; *Chin. J. Chem. Eng.* **2015**, *23*, 1307.
5. Santos, S. C. R.; Boaventura, R. A. R.; *J. Environ. Chem. Eng.* **2016**, *4*, 1473.
6. Shajahan, A.; Shankar, S.; Sathiyaseelan, A.; Narayan, K. S.; Narayanan, V.; Kaviyarasan, V.; Ignacimuthu, S.; *Int. J. Biol. Macromol.* **2017**, *104*, 1449.
7. Uddin, M. K.; Baig, U.; *J. Cleaner Prod.* **2019**, *221*, 1141.
8. Tammina, S. K.; Mandal, B. K.; Kadiyala, N. K.; *Environmental Nanotechnology, Monitoring and Management* **2018**, *10*, 339.
9. Turhan, K.; Turgut, Z.; *Desalination* **2009**, *242*, 256.
10. Körbahti, B. K.; Artut, K.; Geçgel, C.; Özer, A.; *Chem. Eng. J.* **2011**, *173*, 677.
11. Jin, J.; Yang, Z.; Xiong, W.; Zhou, Y.; Xu, R.; Zhang, Y.; Cao, J.; Li, X.; Zhou, C. *Sci. Total Environ.* **2019**, *650*, 408.
12. Rida, K.; Bouraoui, S.; Hadnine, S. *Appl. Clay Sci.* **2013**, *83-84*, 99.
13. Hamzeh, Y.; Ashori, A.; Azadeh, E.; Abdulkhani, A.; *Mater. Sci. Eng., C* **2012**, *32*, 1394.
14. Safa, Y.; Bhatti, H. N.; *Desalination* **2011**, *272,* 313.
15. Wang, H-D.; Yang, Q.; Hui Niu, C.; Badea, I.; *Diam. Relat. Mater.* **2012**, *26*, 1.
16. Chen, Y. H.; *J. Non-Cryst. Solids* **2011**, *357*, 136.
17. Malik, R.; Ramteke, D. S.; Wate, S. R.; *Waste Manage.* **2007**, *27*, 1129.

18. Absalan, G.; Asadi, M.; Kamran, S.; Sheikhian, L.; Goltz, D. M.; *J. Hazard. Mater.* **2011**, *192*, 476.
19. Kataria, N.; Garg, V. K.; Jain, M.; Kadirvelu, K.; *Adv. Powder Technol.* **2016**, *27*, 1180.
20. Liang, X.; Zhao, L.; *RSC Adv.* **2012**, *2*, 5485.
21. Singh, S. A.; Vemparala, B.; Madras, G.; *J. Environ. Chem. Eng.* **2015**, *3* (4, Part A), 2684.
22. Gautam, R. K.; Rawat, V.; Banerjee, S.; Sanroman, M. A.; Soni, S.; Singh, S. K.; Chattopadhyaya, M. C.; *J. Mol. Liq.* **2015**, *212*, 227.
23. Lan, S.; Liu, L.; Li, R.; Leng, Z.; Gan, S. *Ind. Eng. Chem. Res.* **2014**, *53*, 3131.
24. Akar, S. T.; Aslan, S.; Akar, T.; *J. Cleaner Prod.* **2018**, *189*, 887.
25. Meshram, P.; Somani, H.; Pandey, B. D.; Mankhand, T. R.; Deveci, H.; Abhilash. *J. Cleaner Prod.* **2017**, *157*, 322.
26. Ebin, B.; Petranikova, M.; Steenari, B-M.; Ekberg, C.; *Waste Manage.* **2016**, 51, 157.
27. Shokri, A.; Pahlevani, F.; Levick, K.; Cole, I.; Sahajwalla, V.; *J. Cleaner Prod.* **2017**, *142*(Part 4), 2586.
28. Farzana, R.; Rajarao, R.; Hassan, K.; Behera, P. R.; Sahajwalla, V.; *J. Cleaner Prod.* **2018**, *196*, 478.
29. López, F. A.; Cebriano, T.; García-Díaz, I.; Fernández, P.; Rodríguez, O.; Fernández, A. L.; *J. Cleaner Prod.* **2017**, *148*, 795.
30. Deep, A.; Sharma, A. L.; Mohanta, G. C.; Kumar, P.; Kim, K-H.; *Waste Manage.* **2016**, *51*, 190.
31. Valadares, A.; Valadares, C. F.; de Lemos L. R.; Mageste, A. B.; Rodrigues, G. D.; *Hydrometallurgy* **2018**, *181*, 180.
32. Leite, D. D. S; Carvalho, P. L. G.; Lemos, L. R.; Mageste, A. B.; Rodrigues, G. D.; *Sep. Purif. Technol.* **2019**, *210*, 327.
33. Calvete, T.; Lima, E. C.; Cardoso, N. F.; Dias, S. L. P.; Pavan, F. A.; *Chem. Eng. J.* **2009**, *155*, 627.
34. Granata, G.; Pagnanelli, F.; Moscardini, E.; Takacova, Z.; Havlik, T.; Toro, L. *J. Power Sources* **2012**, *212*, 205.
35. Rodrigues, L. E. O. C.; Mansur, M. B.; *J. Power Sources* **2010**, *195*, 3735.
36. Vassura, I.; Morselli, L.; Bernardi, E.; Passarini, F.; *Waste Manage.* **2009**; *29*, 2332.
37. Chen, T.; Sun, Y.; Guo, M.; Zhang, M.; *J. Alloys Compd.* **2018**, *766*, 229.
38. Hu, P.; Chen, Z-Y.; Chang, T.; Deng, J.; Yang, F.; Wang, K-S.; Li, Q-W.; Hu, B-L.; Yu, H-l.; Wang, W-P.; *J. Alloys Compd.* **2017**, *727*, 332.
39. Lua, A. C.; Wang, H. Y.; *Appl. Catal., B* **2014**, *156-157*, 84.
40. Yu, Y.; Chan, Y. M.; Bian, Z.; Song, F.; Wang, J.; Zhong, Q.; Kawi, S.; *Int. J. Hydrogen Energy* **2018**, *43*, 15191.
41. Mironova-Ulmane, N.; Kuzmin, A.; Grube, M.; *J. Alloys Compd.* **2009**, *480*, 97.
42. Wang, J. B.; Huang, G. J.; Zhong, X. L.; Sun, L. Z.; Zhou, Y. C.; Liu, E. H.; *Appl. Phys Lett.* **2006**, *89*, 059901.
43. Julien, C.; Massot, M.; Baddour-Hadjean, R.; Franger, S.; Bach, S.; Pereira-Ramos, J. P.; *Solid State Ionics* **2003**, *159*, 345.
44. Silambarasan, M.; Saravanan, S.; Soga, T.; *e-Journal of Surface Science and Nanotechnology* **2014**, *12*, 283.
45. Ahmad, H. B.; Abbas, Y.; Hussain, M.; Akhtar, N.; Ansari, T. M.; Zuber, M.; Zia, K. M.; Arain, S. A.; *Korean J. Chem. Eng.* **2014**, *31*, 284.
46. Li, N.; Tian, Y.; Zhao, J.; Zhang, J.; Zhang, J.; Zuo, W.; Ding, Y.; *Appl. Catal., B* **2017**, *214*, 126.
47. Tzvetkov, G.; Kaneva, N.; Spassov, T.; *Appl. Surf. Sci* .**2017**, *400*, 481.
48. Huang, C-C.; Lo, S-L.; Lien, H-L.; *Chem. Eng. J.* **2012**, *203*, 95.
49. Tabrizian, P.; Ma, W.; Bakr, A.; Rahaman, M. S.; *J. Colloid Interface Sci.* **2019**, *534*, 549.
50. Lara-Vásquez, E. J.; Solache-Ríos, M.; Gutiérrez-Segura, E.; *J. Environ. Chem. Eng.* **2016**, *4*, 1594.
51. Marcelo, C. R.; Puiatti, G. A.; Nascimento, M. A.; Oliveira, A. F.; Lopes, R. P.; *J. Nanomater.* **2018**. https://doi.org/10.1155/2018/4642038.
52. Dong, G.; Ai, Z.; Zhang, L.; *Water Res.* **2014**, *66*, 22.
53. Zhang, F.; Chen, X.; Wu, F.; Ji, Y.; *Colloids Surf., A* **2016**, *509*, 474.
54. Salter-Blanc, A. J.; Tratnyek, P. G.; *Environ. Sci. Technol.* **2011**, *45*, 4073.
55. Li, H.; Guo, J.; Yang, L.; Lan, Y.; *Sep. Purif. Technol.* **2014**, *132*, 168.
56. Zhang, X. G.; *Corrosion and Electrochemistry of Zinc*, Springer: New York, 1996.
57. Darwish, A. A. A.; Rashad, M.; Al-Aoh, H. A.; *Dyes Pigments* **2019**, *160,* 563.
58. Wang, R.; Li, Q.; Xie, D.; Xiao, H.; Lu, H.; *Appl. Surf. Sci.* **2013**, *279*, 129.
59. Bhowmik, K. L.; Debnath, A.; Nath, R. K.; Das, S.; Chattopadhyay, K. K.; Saha, B.; *J. Mol. Liq.* **2016**, *219*, 1010.
60. Crini, G.; Badot, P-M.; *Prog. Polym. Sci* .**2008**, *33*, 399.
61. Sun, D.; Zhang, Z.; Wang, M.; Wu, W.; *Am. J. Anal. Chem.* **2013**, *4*, 17.
62. Ullhyan, A.; *Global Journal of Biology, Agriculture & Health Sciences* **2014**, *3*, 98.
63. Vakili, M.; Rafatullah, M.; Salamatinia, B.; Ibrahim, M. H.; Abdullah, A. Z.; *Carbohydr. Polym.* **2015**, *132*, 89.
64. Vakili, M.; Rafatullah, M.; Ibrahim, M. H.; Abdullah, A. Z.; Salamatinia, B.; Gholami, Z.; *Carbohydr. Polym.* **2016**, *137*, 139.